Contents lists available at ScienceDirect

Applied Catalysis B: Environmental

Facile preparation of nitrogen and fluorine codoped TiO₂ mesocrystal with visible light photocatalytic activity

Ossama Elbanna, Peng Zhang, Mamoru Fujitsuka, Tetsuro Majima*

The Institute of Scientific and Industrial Research (SANKEN), Osaka University, Mihogaoka 8-1, Ibaraki Osaka 567-0047, Japan

ARTICLE INFO

ABSTRACT

N-doped TiO₂ mesocrystal was prepared through simple hydrothermal treatment with triethanolamine, while F-doped TiO₂ mesocrystal was easily prepared by simple stirring of TiO₂ mesocrystal with NaF at room temperature. The crystal structure and surface area of TiO₂ mesocrystal were not affected by the N- and F-doping. The prepared samples were characterized by X-ray diffraction (XRD), N₂ adsorption, scanning electron microscopy (SEM), transmission electron microscopy (TEM) and UV–vis diffuse reflectance spectroscopy. N,F-codoped TiO₂ mesocrystal showed the highest photocatalytic activity for the degradation of Rhodamine B (RHB) and 4-nitrophenol (4-NP) under the visible light irradiation in 90% and 62% yield, respectively, suggesting the importance of the midgap level due to N 2p above the valence band, and the synergetic effect of N and F doping. Femtosecond time-resolved diffuse reflectance (TDR) spectroscopy was used to clarify the charge-separation, trapping and recombination mechanism, indicating an important role of F for increasing the photocatalytic activity.

© 2016 Elsevier B.V. All rights reserved.

1. Introduction

The preparation of photocatalysts with the high activity of the decomposition of organic pollutants and the production of H₂ by water splitting under the visible light irradiation is one of the main subjects for the development of photocatalysis. TiO₂ is still the most promising photocatalyst due to its high efficiency, low cost, chemical inertness and photostability [1,2]. However, the wide spread use of TiO₂ as photocatalyst has been hampered by its wide band gap which requires ultraviolet irradiation for photocatalytic activation. Since the UV light represents only small fraction ($\sim$5%) of the sun's energy compared to the visible region (45%), TiO₂ can not act as an outstanding photocatalyst under solar light [3]. Therefore, to improve the photocatalytic activity of TiO₂ under the visible light irradiation, significant efforts have been made to prepare metal- and nonmetal-doped TiO₂. The metal-doped TiO₂ exhibits higher thermal instability than nonmetal-doped TiO₂. Also, the substitutional elements act as electron acceptor, resulting in lower photocatalytic efficiency [4,5]. Among different nonmetal-doped TiO₂, N-doped TiO₂ has attracted great attention since the work of Asahi et al. in 2001 that initiated an enormous effort to prepare TiO₂ doped with p-block elements in order to attain the visible light

photocatalytic activity [6]. There is still controversy on the origin of the visible light photoactivity in N-TiO₂. Asahi et al. assumed that doped N atoms narrowed the band gap of TiO₂ by mixing the N 2p and O 2p states which enabled it to absorb the visible light. However, Ihara et al. [7] proposed that the oxygen vacancies contributed to the visible light activity and that the doped N atoms only enhance the stabilization of these oxygen vacancies. F-doped TiO₂ has been examined regarding to doping or surface complexation. Minero et al. studied the photocatalytic decomposition of phenol in aqueous solution over F-doped TiO₂. They found that the photocatalytic degradation of phenol was four times higher than unmodified Deguass P25 which was ascribed to enhance production of hydroxyl radical over F-doped TiO₂ [8]. Recently, many research groups report the enhanced synergetic effect in N,F-codoped such as introduction of new photoactive center, modifying the surface characteristics and tuning the band structure [9].

Mesocrystals, a new class of ordered nanoparticles superstructure were found firstly in biominerals and proposed by Coelfen and Antonietti in 2005 [10]. Mesocrystals are composed of crystalline nanoparticles with a mutual orientation between the nanocrystals building units. Anatase TiO₂ mesocrystal (TMC) superstructure could strongly enhance charge separation under the UV light irradiation resulting in long-lived charges and consequently higher photo conductivities and photocatalytic activities [11]. However, considerable effort was exerted on the preparation of TMC, less work was done on non-metal doping TMC. Up to now, variety of
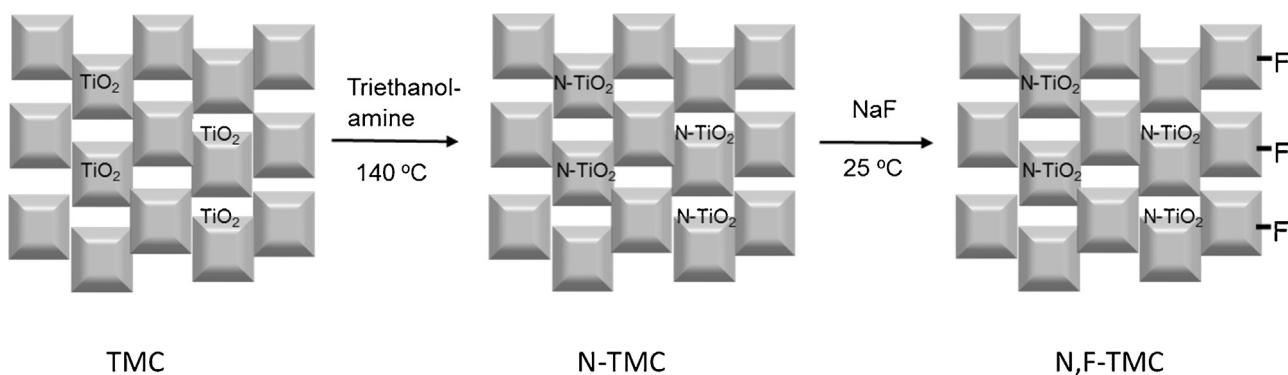
Fig. 1. Schematic illustration of preparation of N-TMC and N,F-TMC.

methods have been used for preparation of N-doped TiO_2 such as sol-gel route [12], chemical vapor deposition [13], spray pyrolysis and ion implantation [14]. Also many papers reported preparation of N-doped TiO_2 by annealing of TiO_2 at a high temperature under NH_3 flow [15]. However, most of these methods need to be conducted at a high temperature which cause low surface area due to particle agglomeration, pore collapse and resulted in low concentration of N. In this paper, we report a simple preparation of N,F-codoped TMC without changing the morphology, crystalline structure, and surface area of TMC. Our method was based on simple hydrothermal treatment of TMC with triethanolamine to prepare N-TMC (Fig. 1). The ordered superstructure of TMC and its high surface area allowed diffusion of N between pores and its adsorption on the surface. The treatment of TMC or N-TMC with NaF resulted in surface fluorination through simple ligand exchange between fluoride anions (F^-) and surface hydroxyl groups on TiO_2 [8].

The photocatalytic degradation of 4-NP and RHB was selected as a probe reaction to measure the photocatalytic activity of the prepared samples under the visible and UV light irradiation. The N,F-codoped TMC showed high activity under the visible light irradiation, while F-doped TMC exhibited high activity under the UV light irradiation.

2. Experimental

2.1. Materials

The titanium (IV) fluoride, sodium fluoride and triethanolamine were purchased from Sigma-Aldrich. The ammonium nitrate and ammonium fluoride were purchased from Wako Pure Chemical Industries. All of these chemicals were analytical grade and used as received.

2.2. Preparation of TMC and doped TMC

TMC was prepared according to our previous report [16], a precursor solution of TiF_4, H_2O, NH_4NO_3 and NH_4F (molar ratio = 1:117:6.6:4) was placed on a silicon wafer to form a thin layer. The precursor was calcined in air using a heating rate of 10 °C/min at 500 °C for 2 h. Moreover, the obtained samples were calcined at 500 °C in oxygen atmosphere for 8 h to ensure removal of surface residue. The N-doped TMC (N-TMC) was prepared using hydrothermal method: 0.2 g TMC was added to 20 mL triethanolamine (Fig. 1). Then, the mixture was exposed to high-intensity ultrasound irradiation for 30 min to disperse it homogenously. After that, the solution was inserted into a Teflon-lined stainless autoclave and was heated at 140 °C for 12 h. After cooling to room temperature, washing with distilled H_2O and ethanol for several times, centrifugation, the precipitate was dried at 200 °C in

air for 12 h. For preparation of F doped TMC (F-TMC), 100 mL aqueous NaF solution with concentration of 50 mM (pH of solution was controlled using HCl (0.1 M)) was added to 0.2 g of TMC and the solution were stirred for 12 h, then washed with distilled water, centrifugation and the precipitate was dried at 100 °C for 12 h. Two codoped samples were prepared. F,N-TMC was prepared by treating F-TMC with triethanolamine following the same procedure used in preparation of N-TMC. N,F-TMC was prepared by treating N-TMC with NaF following the same method for preparation of F-TMC.

2.3. Characterization

X-ray diffraction (XRD) (Rigaku, Smartlab operated at 40 kV and 200 mA, Cu Kα source) was used to examine the crystal structure of the samples. The morphologies were observed using field-emission scanning electron microscopy (FESEM) (JEOL, JSM-6330FT) and transmission electron microscopy (TEM) (JEOL, JEM-2100 operated at 200 kV). The Brunauer–Emmett–Teller (BET) equation was used to calculate the surface area from the adsorption data in the relative pressure range of $P/P_0 = (0.01–0.30)$ (BEL Japan, BELSORP max). The pore volumes and pore diameter distributions were calculated from the adsorption isotherms using the Barrett–Joyner–Halenda (BJH) model. The UV–vis diffuse reflectance spectra (UV-vis DRS) were recorded on a UV–vis spectrophotometer (UV-3100, Shimadzu, Japan) with an integrated sphere attachment using $BaSO_4$ as the reflectance standard. Photoluminescence (PL) emission spectra, was measured at room temperature under the excitation at 325 nm. The surface composition and chemical environment of the prepared samples were analyzed by X-ray photoelectron spectroscopy (XPS). The XPS measurements were carried out with a Kratos Axis 165 spectrometer using a monochromatic Al Kα X-ray. XPS measurements were performed with the spectrometer pass energy set to 80 eV, and the monochromatic Al Kα X-ray source was operated at 150 W.

2.4. Time-resolved diffuse reflectance spectral measurements

The femtosecond diffuse reflectance spectra (TDR) were measured by the pump and probe method using a regeneratively amplified titanium sapphire laser (Spectra-Physics, Spitfire Pro F, 1 kHz) pumped by a Nd:YLF laser (Spectra-Physics, Empower 15). The seed pulse was generated by a titanium sapphire laser (Spectra-Physics, Mai Tai VFSJW; fwhm 80 fs). The fourth harmonic generation (330 or 440 nm, 3 μJ/pulse) of the optical parametric amplifier (Spectra-Physics, OPA-800CF-1) was used as the excitation pulse. The white light continuum pulse, which was generated by focusing the residual of the fundamental light on a sapphire crystal after the computer controlled optical delay, was divided into two parts and was used as the probe and reference lights, of which the

Table 1
The structural characteristics of TMC and doped TMC.

Sample	Surface area (m^2/g)	Pore size (nm)	Pore volume (cm^3/g)	Particle size (nm)
TMC	62.5	15.9	0.25	38.6
N-TMC	58.3	15.9	0.24	40.1
F-TMC	60.1	15.9	0.24	38.6
F,N-TMC	59.3	15.9	0.25	38.0
N,F-TMC	59.7	15.9	0.24	39.0

latter was used to compensate the laser fluctuation. Both the probe and reference lights were directed to the sample powder coated on the glass substrate and the reflected lights were detected by a linear InGaAs array detector equipped with the polychromator (Solar, MS3504). The pump pulse was chopped by the mechanical chopper synchronized to one-half of the laser repetition rate, resulting in a pair of spectra with and without the pump, from which the absorption change (% Abs) induced by the pump pulse was estimated. All measurements were carried out at room temperature.

2.5. Photocatalytic test

The photocatalytic activity was estimated by measuring the degradation of Rhodamine B (RHB) (10 mg/L) and 4-nitrophenol (4-NP) (15 mg/L) under the UV and visible light irradiation. UV-LED source (POT-365; 100 mW cm^{-2}) was used and Xenon lamp (HAL-320; 200 mW cm^{-2}) with UV cut-off filter (λ > 420 nm) was used as the visible light source at room temperature. 50 mg of as-prepared sample was added into 50 mL of RHB solution or 4-NP solution in a 100 mL quartz tube and sonicated for 5 min. Then, the suspension was stirred in dark for 2 h to attain the adsorption–desorption equilibrium on the surface of the catalyst. At the given time intervals, approximately 3 mL of the dispersion was sampled and centrifuged. The filtrates were analyzed by recording variations in the absorption in UV–vis spectra at the characteristics wavelength of RHB and 4-NP. To clarify the involvement of hydroxyl radicals during the photocatalytic reaction, *tert*-butyl alcohol (TBA, 10 mM) as •OH radical scavenger was added to the photocatalytic degradation of RHB and 4-NP over TMC and doped TMC.

3. Results and discussion

3.1. XRD analysis

The XRD patterns of TMC and doped TMC are shown in (Fig. S1) revealing the main anatase peaks at 25.3, 38.0, 48.0, 54.1, 55.0, 62.7, 68.9 and 70.2°, corresponding to the (101), (004), (200), (105), (211), (204), (116) and (220) planes, respectively [17]. The crystallite sizes of different samples were calculated using Scherer's equation from the major diffraction peak (101). Neither new diffraction peak nor change of the position of the characteristic peak of anatase TiO$_2$ shows that the N and F doping on TMC do not change the crystalline structure. Also, the values of the crystallite sizes of TMC and doped TMC in Table 1 are nearly the same. Therefore, the substitutional doping of O by N was not attained because the ionic radius of N ion (171 pm) is much larger than that of O (140 pm). It has been reported that a clear change in crystallite size and lattice parameter happens when O in the lattice is substituted by N [18].

3.2. SEM and TEM analyses

SEM shows that TMC and N-TMC have plate-like structure with size of several micrometers (Fig. 2). TEM images show that TMC, N-TMC and F-TMC have porous structures, indicating that voids exist in the plate (Fig. 3). HRTEM reveals that single crystal lattice exhibits atomic plane of anatase (200) or (020) with the lattice spac-

ing around 0.189 nm [19]. Therefore, we assume that anisotropic growth was preferred to occur in [100] and [010] directions lead to the exposure of {001} facets. Selected area electron diffraction (SAED) can be indexed into diffraction spot corresponding to single crystal anatase along the [001] axis (Fig. S2).

3.3. Nitrogen physical adsorption

As shown in (Fig. S3), the N$_2$ adsorption-desorption isotherms are type II exhibiting hysteresis loop at a high relative pressure between 0.8 and 1 indicating the presence of mesopores. The type II adsorption isotherm is often observed when multi molecular adsorption occurs on a nanoporous solid [20]. Clear pore size distribution with maximum pore radius of 15 nm is observed in all samples. TMC has surface area approximately 62.5 while for N-TMC, F-TMC, F,N-TMC and N,F-TMC are 58.3, 60.1, 59.3 and 59.7 m^2/g, respectively (Table 1), which are larger than 17.7 m^2/g for N-F codoped TMC prepared during the topochemical transformation [21]. The result together with those of XRD, SEM and TEM confirm that this facile preparation of N,F-TMC by post modification has no effect on the morphology and crystal structure of TMC. On the other hand, it is suggested that TiO$_2$ nanoparticles fused slightly for N-F codoped TMC prepared during the topochemical transformation.

3.4. UV–vis absorption spectra and photoluminescence analysis

The UV–vis diffuse reflectance spectra of TMC and doped TMC were measured (Fig. 4a). No absorption was observed for TMC in the visible light region. The F doping showed no change in the fundamental absorption edge of TMC, which is consistent with F-doped TiO$_2$ reported by Yamkai et al. [22]. When N atoms were doped in TMC, the absorption spectrum showed a shoulder peak at the longer wavelength due to the doped N atoms and oxygen vacancies in the lattice with the local electronic states near the valence band edge of TMC. While doping of N atoms into F-TMC (F,N-TMC) resulted in slight decrease of the shoulder absorption compared with N-TMC, indicating that F in F-TMC restricted for a little extent the doping of N. F doping in N-TMC (N,F-TMC) has weak shoulder absorption, indicating the removal of N atoms during F doping. These results are consistent with XPS results as shown below. The band gap energy was calculated by plotting $(\alpha h v)^{1/2}$ versus hv (Fig. 4b). The absorption coefficient and indirect band gap (E_g) relate to Tauc plot $(\alpha h v)^{1/2} \propto h v - E_g$ where v and h are the frequency and Planck's constant, respectively [23]. For pure TMC, the band gap value is 3.08 eV which is close to the expected value of anatase. The midgap energy level due to N doping is 2.15 eV in N-TMC, while it is 2.7 eV in N,F-TMC with lower concentration of N. It is indicated that the visible light absorption and midgap energy level depend mainly on the N concentration in N-TMC and N,F-TMC.

Photoluminescence analysis (PL) have been widely used to understand the fate of electron–hole pairs in semiconductor particles. It is known that the PL emission is resulted from the recombination of excited electrons and holes, the lower PL intensity may indicate the lower recombination rate of electron–holes under light irradiation [23]. As shown in (Fig. S5) TMC has the highest intensity indicating the faster recombination of electrons and
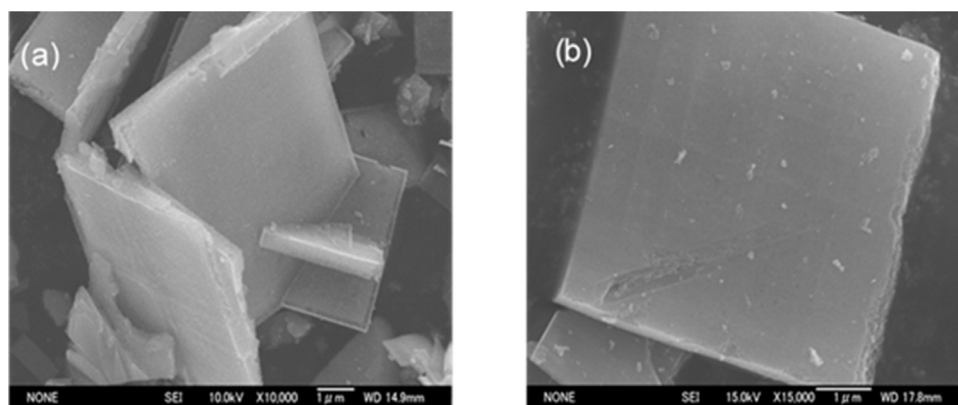
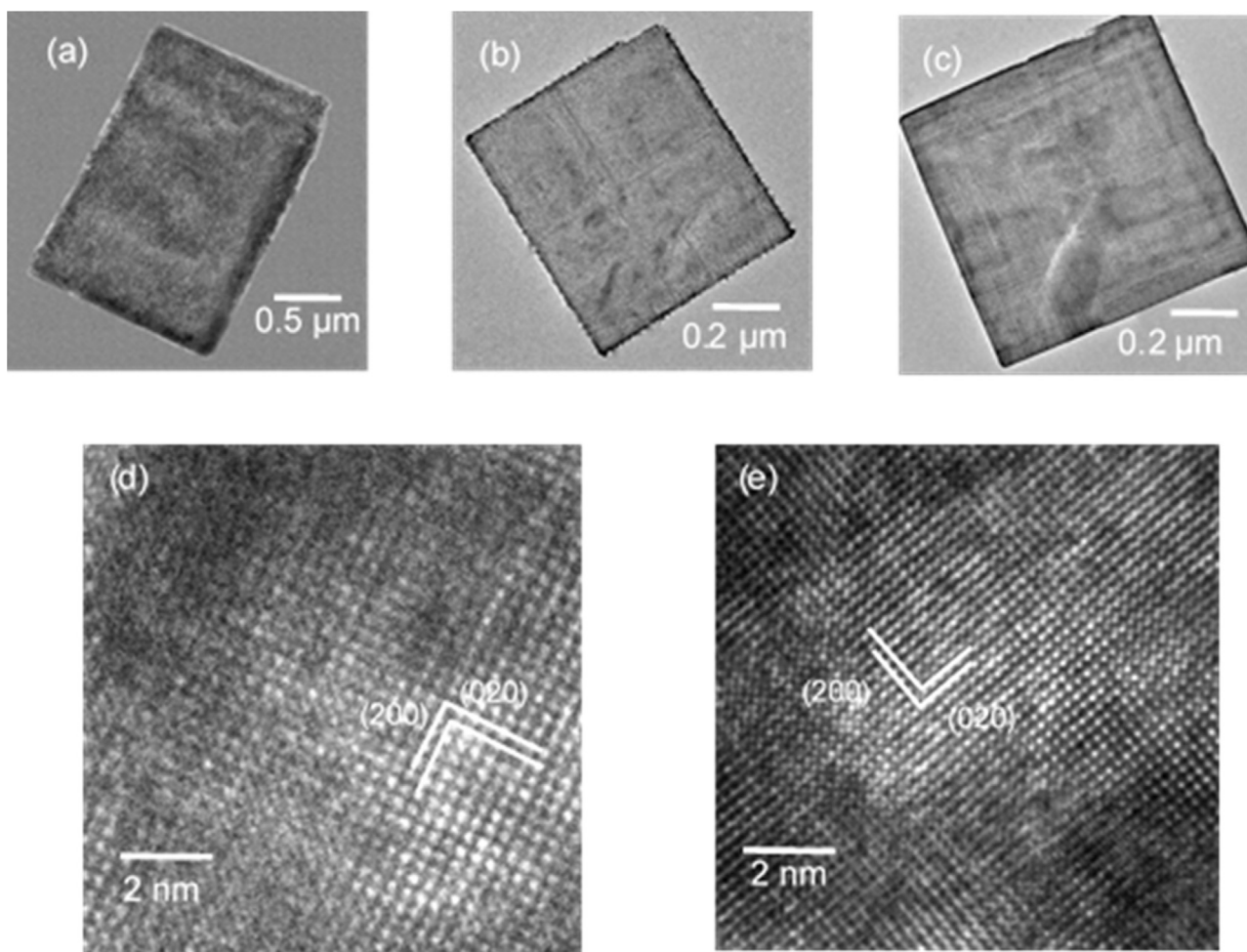**Fig. 2.** SEM images of TMC (a) and N-TMC (b), scale bars 1 μm.

Fig. 3. TEM images of TMC, N-TMC and F-TMC (a–c). HRTEM images of TMC and N-TMC (d and e).

holes. N-TMC and F,N-TMC show slight decrease in PL intensity. F-TMC and N,F-TMC shows efficient quenching of photolumiscence because of electrons can be attracted to F adsorbed on the surface which act as electron trapping site and enhance the charge separation.

3.5. XPS analysis

XPS was performed to elucidate the electronic state and concentration of doped atoms. The photoelectron peak for Ti 2p in Fig. 5c consists of two peaks: one is ascribed to Ti $2p_{3/2}$ at 459.2 eV for pure anatase TiO_2, while the other is to Ti $2p_{1/2}$ at 465 eV with spilt of 5.8 eV to the doublet which is the characteristic of Ti^{4+} in pure anatase TiO_2 [24]. According to Fig. 5a, N 1s binding energy is positioned at 400–401 eV. There is no peak at 396 eV which is assigned to N in Ti—N bond [25]. Since the peak of N at 399–401 eV has been assigned to the incorporated interstitial N of Ti—N—O or Ti—O—N in the TiO_2 lattice [26], the peak at 400–401 eV observed in N-, N,F- and F,N-TMC is assigned to the incorporated interstitial N.

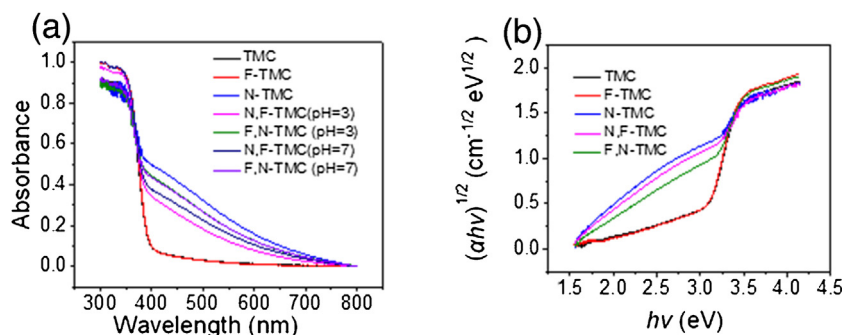**Fig. 4.** UV–vis diffuse reflectance spectra (a) and Tauc plots (b) for TMC and doped TMC.
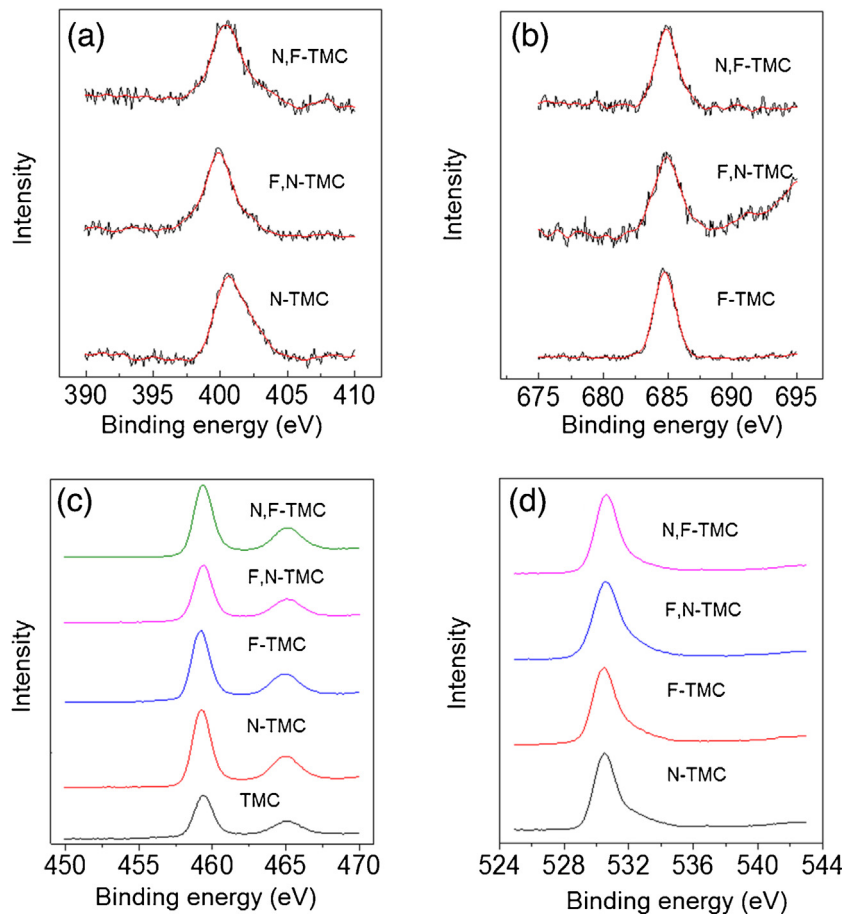

Fig. 5. High-resolution XPS spectra of TMC and doped TMC. N 1s (a), F 1s (b), Ti 2p (c) O 1s regions (d).

Based on the XPS results, the atomic content of N in N-TMC was calculated to be 1.65 where the atomic content of N decreased slightly to 1.54 in the case of F,N-TMC, showing that the F content in F-TMC has less influence on the N doping process. However, the atomic content of N decreased greatly to 0.85 in N,F-TMC, indicating molecularly chemisorbed N in N-TMC was replaced by F. According to these results, the peak of N at 400–401 eV is assigned to not only interstitial N in the TiO_2 lattice but also molecularly chemisorbed N. During F doping in N-TMC, the molecularly chemisorbed N was replaced by F, while the incorporated interstitial N in the TiO_2 lattice conserved its position in the crystal lattice of TMC.

As shown in Fig. 5b, sample F-TMC, F,N-TMC and N,F-TMC have F 1s peak at 684.7 eV due to the surface fluoride (Ti–F) formed by ligand exchange reaction between F$^-$ and surface OH group on the TiO_2 surface [27]. According to the XPS results, the F concentration

decreased from 2.38 in F-TMC to 1.62 in N,F-TMC, indicating that the presence of N limited the surface fluorination. Fig. 5d presents XPS spectra for the O 1s region which shows mainly one peak at 530 eV to be attributed to Ti—O in TiO_2.

3.6. Photocatalytic activity

Fig. 6 exhibited the photocatalytic degradation of RHB and 4-NP under the UV and visible light irradiation where neither RHB nor 4-NP has absorption. As shown in Fig. S5 only small amount of RHB and 4-NP was adsorbed on the surface of TMC and doped TMC before irradiation with the visible or UV light. The degradation yields of RHB and 4-NP on TMC under the visible light irradiation for 5 h are low (6 and 1.1%, respectively). In contrast to TMC, N-TMC showed remarkably high photocatalytic activity of 68 and 33%
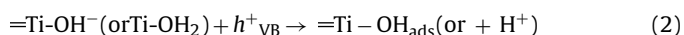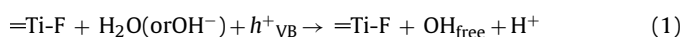
Table 2
The rate constant of RHB and 4-NP degradation (k), band gap and mid-gap level energy, N and F contents in TMC and doped TMC.

Sample	k (/min) for 4-NP, visible light irr.	k (/min) for RHB, visible light irr.	k (/min) for RHB, UV light irr.	Band gap and mid-gap level energy (eV)	N%	F%
TMC	0.4×10^{-4}	2.0×10^{-4}	4.0×10^{-2}	3.07	0	0
N-TMC	13×10^{-4}	30×10^{-4}	2.0×10^{-2}	2.15	1.65	.04
F-TMC	5.0×10^{-4}	5×10^{-4}	5.0×10^{-2}	3.05	0.02	2.38
F,N-TMC	17×10^{-4}	45×10^{-4}	3.5×10^{-2}	2.19	1.54	0.99
N,F-TMC	32×10^{-4}	56×10^{-4}	3.8×10^{-2}	2.70	0.85	1.62
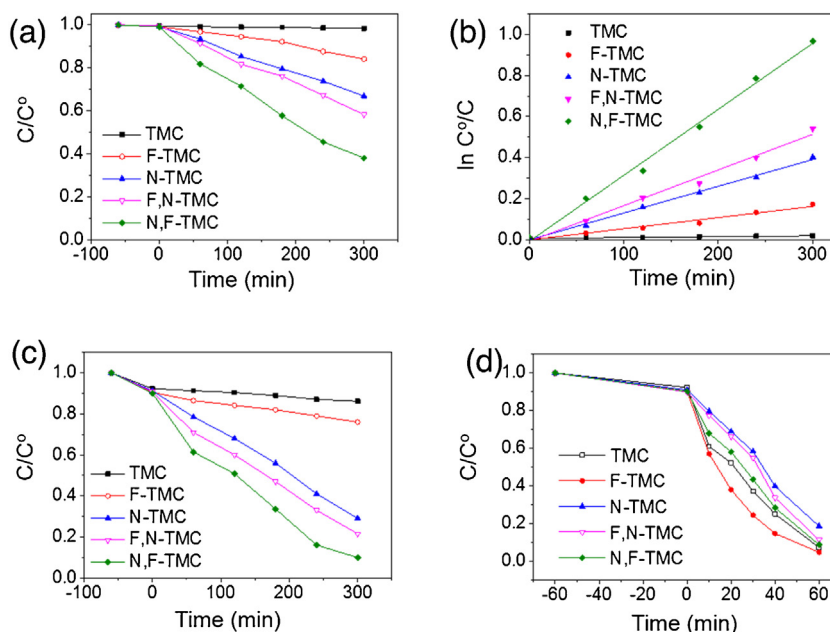
Fig. 6. Photocatalytic degradation of 4-NP under the visible light irradiation (a), kinetic linear fitting of degradation of 4-NP under the visible light irradiation (b), photocatalytic degradation of RHB under the visible (c) and UV light irradiation (d).

for the degradation of RHB and 4-NP, respectively, because of the visible-light absorption of N-TMC with the midgap energy level.

Although F-TMC has no absorption in the visible light region, F-TMC showed the photocatalytic activity of 24 and 16% for degradation of RHB and 4-NP, respectively. The photocatalytic activity can be explained by the high surface acidity because of F doping enhanced the adsorption of organic molecules on the surface of F-TMC. In addition, it has been reported that F doping enhances the generation of free hydroxyl radicals (OH_{free}) in F-TMC (Eq. (1)) [28], while hydroxyl radicals are formed to be adsorbed on the surface (OH_{ads}) via the oxidation of OH^- adsorbed on the surface of TMC (Eq. (2)), inducing much less reactivity than OH_{free}.

$$\equiv Ti\text{-}F + H_2O(orOH^-) + h^+{}_{VB} \rightarrow \ \equiv Ti\text{-}F + OH_{free} + H^+ \tag{1}$$

$$\equiv Ti\text{-}OH^-(orTi\text{-}OH_2) + h^+{}_{VB} \rightarrow \ \equiv Ti - OH_{ads}(or + H^+) \tag{2}$$

Moreover, the photocatalytic activity of F-TMC under the visible light can be explained due to photoexcitation of extrinsic absorption bands. The extrinsic absorption originates from the photoionization of original or newly formed defects and the excitation of surface states. Such extrinsic absorption requires less energy to activate. Thus, it is possible to generate free charge carriers to induce surface chemical reactions under the visible light irradiation [29].

Interestingly, N,F-TMC showed the highest photocatalytic activity with the degradation yields of 90 and 62% for the degradation of RHB and 4NP, respectively. The result may be attributed to synergetic effect of N and F. N is responsible for the absorption in

Table 3
Kinetic parameters, lifetimes (τ_1, τ_2 and τ_3 in ps) and ratios in% of three components, for the charge decay observed for TMC and doped TMC under the visible and UV light irradiation.

Sample	Visible light irradiation			UV light irradiation		
	τ_1 (ps)	τ_2 (ps)	τ_3 (ps)	τ_1 (ps)	τ_2 (ps)	τ_3 (ps)
TMC	0.5 (30%)	25 (25%)	483 (45%)	3.1 (25%)	34 (41%)	292 (34%)
F-TMC	1.5 (20%)	83 (40%)	2286 (40%)	12.5 (36%)	109 (37%)	572 (27%)
N-TMC	1.4 (19%)	83 (34%)	2716 (46%)	2.1 (34%)	16 (30%)	351 (36%)
N,F-MC	1.6 (20%)	108 (20%)	5410 (60%)	4.9 (37%)	55 (28%)	405 (35%)

the visible light region, while F enhances the production of OH_{free} through equation (2). On the other hand, F,N-TMC showed lower photocatalytic activity than that for N,F-TMC with 78 and 38% for the degradation of RHB and 4-NP due to high concentration of N which may increase the electron-hole recombination rate and the decrease in concentration of F.

Under the UV light irradiation, F-TMC showed the highest photocatalytic activity due to the stronger absorption of F-TMC in the UV region than TMC, leading to the higher production of OH_{free}. TMC also exhibited high photocatalytic activity under the UV light irradiation, although it showed low activity under the visible light irradiation. N-TMC showed lower (approximately 80%) photocatalytic activity for the degradation of RHB than TMC and F-TMC under the UV light irradiation. N doping generated the oxygen vacancies which increase the electron–hole recombination rate. F,N-TMC and N,F-TMC have high photocatalytic activity of approx-
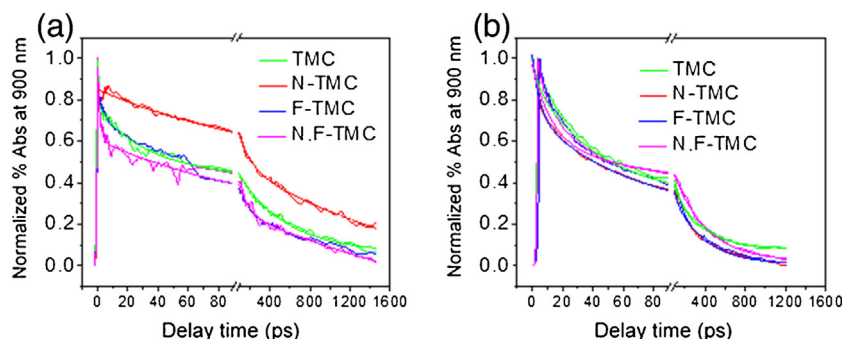
Fig. 7. Time profiles of normalized transient absorption at 900 nm observed after the excitation of TMC and doped TMC at 440 nm (a) and 330 nm (b).
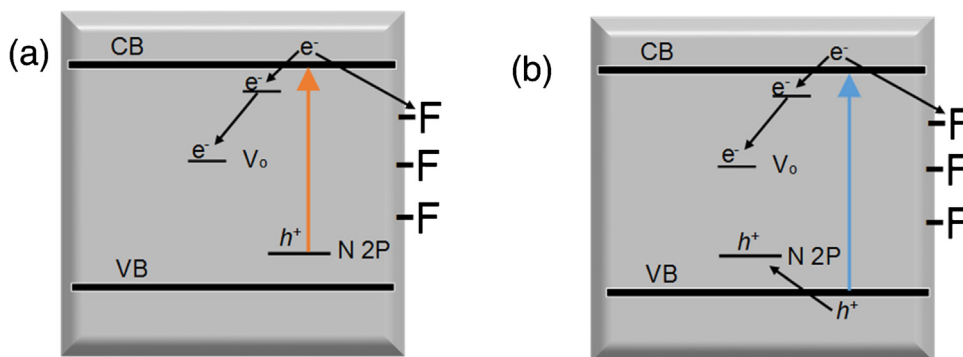

Fig. 8. Schematic illustration of the spatial and energetic distribution of electrons and holes after excitation at 440 nm (a) and 330 nm (b) in N,F-TMC and N-TMC. V_o represents oxygen vacancy site.

imately 88% and 93%, respectively compared with N-TMC for the degradation of RHB due to the decrease in concentration of N and the presence of F. The rate constant for photocatalytic degradation of different samples was calculated through equation: ln $C°/C = kt$ and were summarized in Table 2.

As observed in (Fig. S6) and (Table S1), the degradation efficiencies of RHB and 4-NP are significantly reduced with the addition of •OH scavenger (TBA) which confirmed the important role of hydroxyl radicals in photocatalytic reaction.

In addition to the high photocatalytic activity, N,F-TMC exhibited high stability and durability during the photocatalytic degradation of RHB and 4-NP under the visible light irradiation (Fig. S7). The degradation yield was kept to be nearly 100% for 4-NP and RHB after recycling 4 times.

In general, the photocatalytic activity depends on several factors such as surface area, surface hydroxyl density and oxygen vacancies. The doped TMC with high surface area and the same crystal structure as TMC has advantage to provide abundant reaction sites for photocatalytic reactions and enhance the charge separation. The N and F doping on TMC has strong absorption in the visible light range and increase the production of hydroxyl radicals, respectively, which are responsible for high photocatalytic activity under the visible light and UV light irradiation.

3.7. Charge transfer dynamics on doped TMC

Time resolved diffused reflectance spectroscopy, which is strong analytical tool to examine charge transfer in photocatalysis, was used to clarify the charge transfer dynamic under the visible and UV light irradiation. Upon the 440-nm laser excitation, N-TMC and N,F-TMC showed the broad absorption in the 800–1200 nm region (Fig. S9) which is assigned to the transient absorption of charges generated in N-TMC and N,F-TMC. The transition of Ti 3d ⟵ N 2P happened and both electrons and holes were generated in the CB

and N 2p mid-gap level, respectively [30]. The electrons in the CB were trapped in the defect sites to give trapped electrons ($e^-_{trapped}$) and react with O_2 to give oxygen anion (O_2^-) (Eq. (3)).

$$O_2 + e^-_{trapped} \rightarrow O_2^- \tag{3}$$

On the other hand, the holes were separated and localized at the N 2P state. The electrons and holes decayed in a part by charge recombination. The decay of the charges was analyzed by three-exponential function (Fig. 7) with the lifetimes of 1.6 (τ_1), 108 (τ_2) and 5410 ps (τ_3) for N,F-TMC, while those were 1.4 (τ_1), 80 (τ_2) and 2716 ps (τ_3) for N-TMC (Table 3). τ_1 is assigned for $e^-_{trapped}$ on the trapping site. τ_2 is responsible to the diffusion of $e^-_{trapped}$ to the oxygen vacancy site (V_o). τ_3 is related to the diffusion of $e^-_{trapped}$ to the reaction site for the photocatalytic reaction such as the oxygen reduction (Eq. (3)). Then, $e^-_{trapped}$ disappear by charge recombination with holes localized at the N 2P state.

The longer lifetime of the generated electrons and holes increases the photocatalytic activity because the charge transfer needs to occur at the catalyst surface of the substrates. N,F-TMC with longer lifetime of 1.6 (τ_1), 108 (τ_2) and 5410 ps (τ_3) exhibited higher photocatalytic activity than N-TMC 1.4 (τ_1), 80 (τ_2) and 2716 ps (τ_3). τ_3 of N,F-TMC is almost two times longer than τ_3 of N-TMC, while τ_1 is similar for N,F-TMC and N-TMC. It is suggested that F doping to N-TMC increases τ_3 remarkably.

It is suggested that electrons can be attracted to F adsorbed on the surface due to its high electronegativity (Fig. 8) which decreased the rate of charge recombination and allowed holes to combine with OH^- adsorbed on the surface, leading to the formation of OH (Eq. (4)).

$$OH^- + h^+ \rightarrow OH \tag{4}$$

It has been reported that the F doping induces the formation of long-living luminescent surface trapping sites and enhances the photocatalytic activity because these trapping sites reduce the

undesired electron-hole recombination [31]. However, in the case of N-TMC electrons were deeply trapped on the oxygen vacancies [30] which increased the chance of charge recombination with holes localized in N 2P state and decreased the photocatalytic activity. These results confirm the synergetic effect of N and F. N increases the absorption in the visible light region, while F improves charge separation and prevents electron-hole recombination, leading to increase of the photocatalytic activity.

Under the UV laser excitation at 330 nm, the generated electrons and holes on TMC were usually captured at the surface defects to produce O_2^- with increasing the photocatalytic efficiency. F-TMC exhibited the charge decay with three components lifetimes of 12.5 (τ_1), 109 (τ_2) and 572 ps (τ_3). It is suggested that F adsorbed on the surface attracted photogenerated electrons and increased the photocatalytic efficiency by improving charge separation. On the other hand, N-TMC showed the charge decay with lifetimes of 2.1 (τ_1), 16 (τ_2) and 351 ps (τ_3), and the photocatalytic activity is lower. Since the potential energy of the photoinduced holes decreases in N-TMC, the holes have weaker oxidation power [32]. On the other hand, N,F-TMC showed the charge decay with longer lifetimes of 4.9 (τ_1), 55 (τ_2) and 405 ps (τ_3) and larger photocatalytic activity compared with N-TMC. The difference was attributed to the presence of F in N,F-TMC. These results suggest that the F-doping did not only enhance the production of OH radicals but also improved the charge separation efficiency.

4. Conclusions

N-TMC, F-TMC and N,F-TMC were prepared by the simple post modification. They have plate-like structure and high surface area, indicating that doping has no effect on the crystal structure of TMC. Compared with TMC, N-TMC has shoulder peak at longer wavelength which reveals the remarkably absorption in the visible light region. N,F-TMC has high photocatalytic activity for the degradation of RHB and 4-NP under the visible light irradiation. The high activity of N,F-TMC is attributed to the synergetic effect of N and F doping. The doped N atoms enhance the visible light absorption, leading to a decrease in the band gap energy which is dependent on the concentration of N, while the F increases the production of hydroxyl radicals, adsorption and improve charge separation efficiency.

Appendix A. Supplementary data

Supplementary data associated with this article can be found, in the online version, at http://dx.doi.org/10.1016/j.apcatb.2016.03.053.

References

[1] A. Fujishima, K. Honda, Nature 238 (1972) 37–38.
[2] S. Sakthivel, M. Janczarek, H. Kisch, J. Phys. Chem. B 108 (2004) 19384–19387.
[3] D. Dolata, S. Moziaa, R.J. Wróbela, D. Moszynskia, B. Ohtanib, N. Guskosc, A.W. Morawski, Appl. Catal. B: Environ. 162 (2015) 310–318.
[4] C. Burda, Y. Lou, X. Chen, A.C. Samia, J. Stout, J.L. Gole, Nano Lett. 3 (2003) 1049–1051.
[5] C.D. Valentin, E. Finazzi, G. Pacchioni, A. Selloni, S. Livraghi, M.C. Paganini, E. Giamello, Chem. Phys. 339 (2007) 44–56.
[6] R. Asahi, T. Morikawa, T. Ohwaki, K. Aoki, Y. Taga, Science 293 (2001) 269–271.
[7] T. Ihara, M. Miyoshi, Y. Iriyama, O. Matsumoto, S. Sugihara, Appl. Catal. B: Environ. 42 (2003) 403–409.
[8] C. Minero, G. Mariella, V. Maurino, E. Pelizzetti, Langmuir 16 (2000) 2632–2641.
[9] Y. Zhanga, C. Han, M. Nadagouda, D. Dionysiou, Appl. Catal. B: Environ. 168–169 (2015) 550–558.
[10] H. Coelfen, M. Antonietti, Angew. Chem. Int. Ed. 44 (2005) 5576–5591.
[11] Z. Bian, T. Tachikawa, P. Zhang, M. Fujitsuka, T. Majima, J. Am. Chem. Soc. 136 (2014) 458–465.
[12] Y. Zhang, Z. Zhao, J. Chen, L. Cheng, J. Chang, W. Sheng, C. Hu, S. Cao, Appl. Catal. B 166 (2015) 644.
[13] D. Li, H. Haneda, S. Hishita, N. Ohashi, Chem. Mater. 17 (2005) 2588–2595.
[14] A. Borraís, C. Loípez, V. Rico, F. Gracia, A.R. Gonzaílez-Elipe, E. Richter, G. Battiston, R. Gerbasi, N. McSporran, G. Sauthier, E. Gyo1rgy, A. Figueras, J. Phys. Chem. C. 111 (2007) 1801–1808.
[15] S. Joung, T. Amemiya, M. Murabayashi, K. Itoh, Chem. Eur. J. 12 (2006) 5526–5534.
[16] Z. Bian, T. Tachikawa, M. Fujitsuka, T. Majima, J. Phys. Chem. Lett. 3 (2012) 1422–1427.
[17] J.I. Brauer, G. Szulczewski, J. Phys. Chem. B 118 (2014) 14188–14195.
[18] D. Chen, Z. Jiang, J. Geng, J. Zhu, D. Yang, J. Nanopart Res. 11 (2009) 303–313.
[19] H.G. Yang, C.H. Sun, S.Z. Qiao, J. Zou, G. Liu, S.C. Smith, H.M. Cheng, G.Q. Lu, Nature 453 (2008) 638–641.
[20] S.J. Gregg, K.S.W. Sing, Adsorption, Surface Area Porosity, Academic Press, London, 1997, pp. 111.
[21] P. Zhang, M. Fujitsuka, T. Majima, Appl. Catal. B: Environ. 185 (2016) 181–188.
[22] H. Yamaki, T. Umebayashi, T. Sumita, S. Yamamoto, M. Maekawa, A. Kawasuso, H. Itoh, Nucl. Instrum. Methods Phys. Res. B 306 (2003) 254–258.
[23] J.C. Yu, J.G. Yu, W.K. Ho, Z.T. Jiang, L.Z. Zhang, Chem. Mater. 14 (2002) 3808–3816.
[24] J. Xu, B. Yang, M. Wu, Z. Fu, Y. Lv, Y. Zhao, J. Phys. Chem. C 114 (2010) 15251–15259.
[25] F. Peng, L. Cai, H. Yu, H. Wang, J. Yang, J. Solid State Chem. 181 (2008) 130–136.
[26] G. Liu, H. Gui, Y. Wang, L. Cheng, J. Pan, G. Qing, H. Cheng, J. Am. Chem. Soc. 31 (2009) 12869–12870.
[27] J. Cheng, J. Chen, W. Lin, Y. Liu, Y. Kong, Appl. Surf. Sci. 332 (2015) 573–580.
[28] H. Park, W. Choi, J. Phys. Chem. B 108 (2004) 4086–4093.
[29] D. Li, H. Haneda, N.K. Labhsetwar, S. Hishita, N. Ohashi, Chem. Phys. Lett. 401 (2005) 579–584.
[30] K.I. Yamanaka, T. Morikawa, J. Phys. Chem. C 116 (2012) 1286–1292.
[31] M.V. Dozzi, C. D'Andrea, B. Ohtani, G. Valentini, E. Selli, J. Phys. Chem. C 117 (2013) 25586–25595.
[32] R. Asahi, T. Morikawa, H. Irie, T. Ohwaki, Chem. Rev. 114 (2014) 9824–9852.